MATERIALS SCIENCE

High-density array of ferroelectric nanodots with robust and reversibly switchable topological domain states

Zhongwen Li,[1] Yujia Wang,[2] Guo Tian,[1] Peilian Li,[1] Lina Zhao,[1] Fengyuan Zhang,[1] Junxiang Yao,[1] Hua Fan,[1] Xiao Song,[1] Deyang Chen,[1] Zhen Fan,[1] Minghui Qin,[1] Min Zeng,[1] Zhang Zhang,[1] Xubing Lu,[1] Shejun Hu,[1] Chihou Lei,[3] Qingfeng Zhu,[4] Jiangyu Li,[4,5] Xingsen Gao,[1]* Jun-Ming Liu[1,6]*

The exotic topological domains in ferroelectrics and multiferroics have attracted extensive interest in recent years due to their novel functionalities and potential applications in nanoelectronic devices. One of the key challenges for these applications is a realization of robust yet reversibly switchable nanoscale topological domain states with high density, wherein spontaneous topological structures can be individually addressed and controlled. This has been accomplished in our work using high-density arrays of epitaxial BiFeO$_3$ (BFO) ferroelectric nanodots with a lateral size as small as ~60 nm. We demonstrate various types of spontaneous topological domain structures, including center-convergent domains, center-divergent domains, and double-center domains, which are stable over sufficiently long time but can be manipulated and reversibly switched by electric field. The formation mechanisms of these topological domain states, assisted by the accumulation of compensating charges on the surface, have also been revealed. These results demonstrated that these reversibly switchable topological domain arrays are promising for applications in high-density nanoferroelectric devices such as nonvolatile memories.

INTRODUCTION

Topological structures in ferroics have received substantial attentions in recent years, and a number of exciting discoveries have been reported (1–10). Topological defects are usually considered as some singular regions of low dimensionalities, in which the order parameters cease to vary continuously (2). Two-dimensional (2D) topological defects include the well-known ferroic domain walls that have been extensively investigated for domain wall nanoelectronics (1). 1D defects such as flux-closure vortex and skyrmion states, as schematically shown in fig. S1, have also been the focus of extensive research studies (3–7), and specific center domain patterns were also reported recently (9). These topological domain states, in combination with multiferroic functionalities, may lead to exciting new discoveries and device applications. For example, it was predicted that switchable polar vortex as small as 3.2 nm can remain stable, corresponding to an ultrahigh storage density of 60 Tbit/inch^2 (3).

Although 1D topological defects in ferroelectrics and multiferroics have long been predicted, for example, vortex domains by Naumov et al. (3), their experimental observations remain elusive, in contrast to the well-studied analogs in ferromagnets (1). Recently, experimental evidences especially with flux-closure domain structures have gradually emerged because of the powerful piezoresponse force microscopy (PFM) and advanced transmission electron microscopy (1, 4, 9–19). For example, Nelson et al. (10) and Jia et al. (11) demonstrated the existence of half flux-closure quadrants in BiFeO$_3$ (BFO) and Pb(Zr,Ti)O$_3$

(PZT) thin films, respectively. Multistate vortex-antivortex pairs were revealed in rare earth manganites and other improper ferroelectrics by Cheong and coworkers (6, 14–16). More recently, the periodic array of flux-closure vortices was found in PbTiO$_3$/SrTiO$_3$ multilayers by Tang et al. (12) and in superlattices by Yadav et al. (13). In BFO films, the formation of vortex and antivortex domain structures induced by electric field was also demonstrated by Balke et al. (17, 18). In addition, specific center domain structures can be induced by radial electric field from a scanning probe, as reported by Vasudevan et al. (9) and Chen et al. (19), although no spontaneously formed center domains have been observed. In spite of these tremendous progresses, robust yet switchable topological domain states critical for realizing future nanoelectronics remain elusive.

It is well known that polarization-strain coupling can be relieved in nanoscale ferroelectrics, resulting in more varieties of topological domains in confined systems (20–23). For example, unique domain quadrants and flux-closure quadrants were observed in micrometer-sized single-crystal BaTiO$_3$ lamellae by Schilling et al. (24), McGilly et al. (25), and McQuaid et al. (26). Rodriguez et al. (27) reported evidence for vortex states in small PZT nanodot arrays. These studies suggested that dimension-reduction down to nanoscale is an effective strategy to manipulate topological defects, wherein delicate balances exist among various energetics such as exchanges, electro-elastic interaction, and electrostatic interaction, which are closely related to dimension and surfaces. These findings could pave way toward nanoferroelectronics based on local topological defects, if they are robust and switchable.

Inspired by this vision, we seek to explore possible topological defects (domain states) in the high-density array of epitaxial BFO nanodots. BFO is the most intensively studied multiferroic, promising for rich physics associated with various domain structures in addition to its superior electric properties (28–30). Although vortex and center domain states generated by radial electric field were observed in BFO films, they cannot be spontaneously generated, and their robustness and controllability remain to be seen (9, 18, 19). Here, we demonstrate individually controllable spontaneous center-type topological defects in high-density BFO nanodot arrays, whose emergence does not require the assistance of any

[1]Institute for Advanced Materials and Guangdong Provincial Key Laboratory of Quantum Engineering and Quantum Materials, South China Normal University, Guangzhou 510006, China. [2]Shenyang National Laboratory for Materials Science, Institute of Metal Research, Chinese Academy of Sciences, 72 Wenhua Road, Shenyang 110016, China. [3]Department of Aerospace and Mechanical Engineering, Saint Louis University, St. Louis, MO 63103–1110, USA. [4]Shenzhen Key Laboratory of Nanobiomechanics, Shenzhen Institutes of Advanced Technology, Chinese Academy of Sciences, Shenzhen, Guangdong 518055, China. [5]Department of Mechanical Engineering, University of Washington, Seattle, WA 98195–2600, USA. [6]National Laboratory of Solid State Microstructures and Collaborative Innovation Center of Advanced Microstructures, Nanjing University, Nanjing 21009, China.
*Corresponding author. Email: xingsengao@scnu.edu.cn (X.G.); liujm@nju.edu.cn (J.-M.L.)

external electric field, a distinct advantage over earlier reports (9, 19). Using vector PFM and phase-field simulation, we revealed a large percentage of center-type topological domains in individual nanodots, analog to recently observed hedgehog spin meron states (31). These topological domain states are robust and individually controllable by electric field, a particularly promising characteristic, enabling on-demand manipulation for applications and offering opportunities for further exploration of their novel properties in high-density device applications.

RESULTS

Structural and PFM characterizations of BFO nanodot arrays

The arrayed nanodots under investigation are ~60 nm in lateral dimension and ~30 nm in height, corresponding to a pixel density of ~100 Gbit/inch^2. The fabrication procedure is schematically shown in fig. S2. To synthesize high-quality nanodots, we used a newly developed top-down ion-etching method using sacrificed nanoporous anodic alumina (AAO) template (32), which is different from conventional AAO template methods (33–37). The details of this synthesis can be found in the Supplementary Materials. The scanning electron microscopy (SEM) image (Fig. 1A) shows the well-ordered array of nanodots on the SrTiO₃ substrate. The epitaxial structure of these nanodots was verified by x-ray diffraction (XRD), featured by the (001) and (002) peaks in Fig. 1B. The out-of-plane lattice constant is ~4.03 Å, close to that of rhombohedral BFO films (38, 39).

The domain structures of these nanodots were characterized by PFM (40), noting that the vector PFM functionality allows the simultaneous mapping of vertical (out-of-plane) and lateral (in-plane) amplitudes (V-amp. and L-amp.) and phases (V-pha. and L-pha.) of piezoresponse signals. The V-amp. and V-pha. images shown in Fig. 1 (C and D) for an as-prepared sample exhibit several unique features. Most of the nanodots have dark phase contrast, although some display bright contrast, suggesting the favorable upward vertical polarization component. There are a small number of nanodots showing double contrasts, implying the coexistence of upward and downward polarization components separated by a domain wall in each case. More interesting is the lateral PFM image, and the typical examples are demonstrated in Fig. 1 (E and F), which cover the same area as Fig. 1 (C and D). Some characteristics can be highlighted here. First, most of the nanodots have the half-dark and half-bright contrast in the L-pha. image (Fig. 1F). Besides, a small number of nanodots show even more complicated L-pha. contrast, for example, dark/bright/dark or bright/dark/bright pattern from left to right. These features are verified by the presence of a coarse dark line in the L-amp. image (see Fig. 1E), exhibiting a domain wall–like characteristic for the later polarization component along the <010> direction.

The PFM images for polarization switching induced by applying a scanning electric bias via the atomic force microscopy (AFM) probe are also shown in fig. S3. Distinctly different contrasts in both the vertical and lateral PFM images can be found in the regions poled by the different dc bias voltages for +8 and −8 V, respectively, indicating the concurrent switching of both the vertical and lateral polarization components (see fig. S3, A to D). Moreover, the point-wise polarization reversal was checked on a number of nanodots one by one, and the typical amplitude and phase loops are plotted in fig. S3 (E and F). The square-like phase loop evidences a 180° phase difference, indicating a complete switching of the point-wise vertical polarization with a coercive voltage of ~4 V.

From these PFM images, we can identify different domains, as shown in the enlarged images in the gap between two columns of the PFM images in Fig. 1. The first type (type I) shows the dark/bright contrast in the L-pha. image but the uniform dark contrast in the V-pha. image. The second (type II) exhibits the bright/dark contrast in the L-pha. image and the uniform bright contrast in the V-pha. image, a reversed contrast with respect to type I. Type III shows the dark/bright/dark contrast in the L-pha. image together with the dark/bright double contrasts in the V-pha. image. Type IV shows the reversed contrast to type III, with the bright/dark/bright contrast in the L-pha. image and bright/dark double contrasts in the V-pha. image. The observations thus identify an emergent phenomenon and also raise an important question: What is the polarization distribution in these domains?

Domain structure reconstruction

The above analysis on the lateral PFM images can capture the polarization components along the x and z axes. Given the fact that the polarization may point to any directions in 3D space, a full determination of polarization distribution in an individual nanodot must consult to additional data regarding the y-axis component. This can be performed by combining the PFM data for different in-plane rotational angles of the sample (40–46). Taking the data in Fig. 1 (C to F) as reference where the sample alignment angle is set as 0°, we conducted additional PFM imaging by rotating the sample clockwise for a set of given angles. The complete PFM data for an array of nanodots and the selected individual nanodots at different rotation angles can be found in figs. S4 and S5. Both the topographic and vector PFM images for the same region before
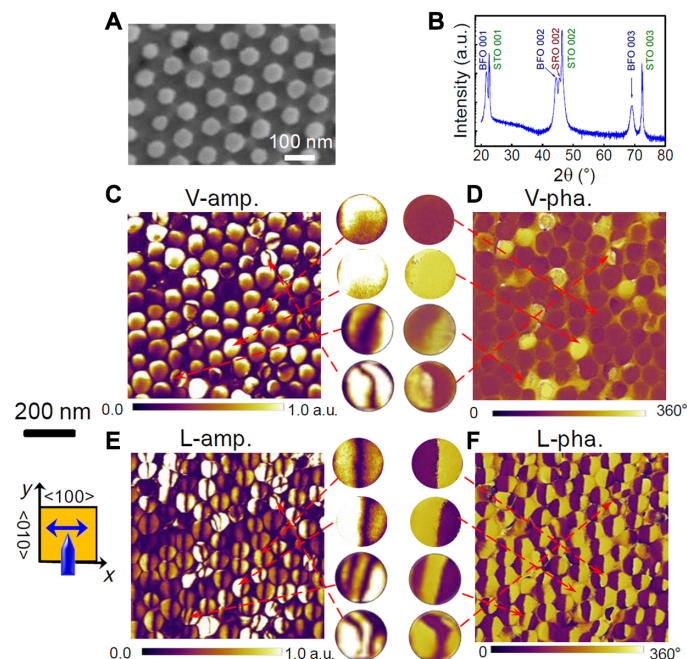

Fig. 1. Structure and PFM images for a BFO nanodot array. (**A**) SEM image. (**B**) XRD pattern. STO, (001)-oriented SrTiO₃; SRO, SrRuO₃; a.u., arbitrary units. (**C** and **D**) Vertical PFM amplitude (V-amp.) (C) and phase (V-pha.) (D) images for the as-prepared nanodot sample. (**E** and **F**) Lateral PFM amplitude (L-amp.) (E) and phase (L-pha.) (F) images. Some single nanodot PFM images are zoomed-in and shown in the insets in the gap between (C) and (D) and (E) and (F), illustrating some typical PFM contrast variants frequently observed in the nanodots. The inset schematic diagram of the cantilever indicates that the cantilever is parallel to the y axis (<010> direction); thus, the contrasts in the lateral PFM image reflect the x components of polarization vectors (along the <100> direction). All the PFM images (C to F) are from the same region.

and after the rotations can match well without apparent image distortion. To resolve the 3D polarization distribution, we conducted a vector PFM mapping following the method proposed by Rodriguez et al. (44) and Kalinin and Gruverman (45).

First, we chose a nanodot with a typical type I PFM contrast as a paradigm, and the construction procedure is demonstrated in Fig. 2. The PFM images (amplitude and phase) for the x component (lateral PFM at an angle of 0°, with the cantilever parallel to the <010> crystallographic direction), y component (lateral PFM at an angle of 90°, for sample clockwise rotation for 90° with the cantilever parallel to the <100> direction), and z component (vertical PFM) are presented in Fig. 2 (A to C). Second, the amplitude and phase images can be converted to the PFM piezoresponse signal contours of the x component (PFMx), y component (PFMy), and z component (PFMz), according to the function $R\cos(\theta)$ (R is the amplitude, and θ is the phase angle), as shown in Fig. 2 (D to G). Finally, the as-evaluated PFMx and PFMy images are converted into the 2D vector contours using the MATLAB programming, as presented in Fig. 2H for the amplitude map and Fig. 2I for the vector angle map, reflecting the local polarization distributions for in-plane components. The 3D vector contours can also be constructed from the PFMx, PFMy, and PFMz data, as demonstrated in Fig. 2 (J and K). From the resulting contours, we are able to identify that this nanodot has a unique domain structure, with all the lateral polarization vectors pointing radially to the center, as schematically illustrated in Fig. 2L, where the vertical components over the whole nanodot are pointing downward. That is the so-called center-type topological domain (2, 9). Such a domain state also matches well with the PFM contrasts obtained after arbitrary angle rotations, for example, by 45°. This domain structure is somewhat similar to the quadrant center domain, as previously reported by Vasudevan et al. (9), created by a large radial electric field in the BFO film via the AFM tip. Notably, our domain structure has its polarizations rotating more or less continuously, indicating a roughly isotropic center domain analog to hedgehog spin topological meron states (31). This specific domain pattern was generated spontaneously in the as-fabricated nanodots without any assistance of an external field. This is a major step toward practical applications, markedly different from the quadrant ones in previous reports (9, 19). The spontaneous occurrence of the center topological domains in the virgin state also implies that they are probably the most stable states, essential for further manipulation and application as a functional unit in devices.

Similar analysis has been conducted on other types of nanodots, and the results are summarized in Fig. 3, with more detailed PFM data presented in fig. S5. Now, it is understood that type I (Fig. 3A) is the radially center-convergent domain, with polarizations pointing inward to the center. Type II (Fig. 3B) shows the uniform dark contrast in the
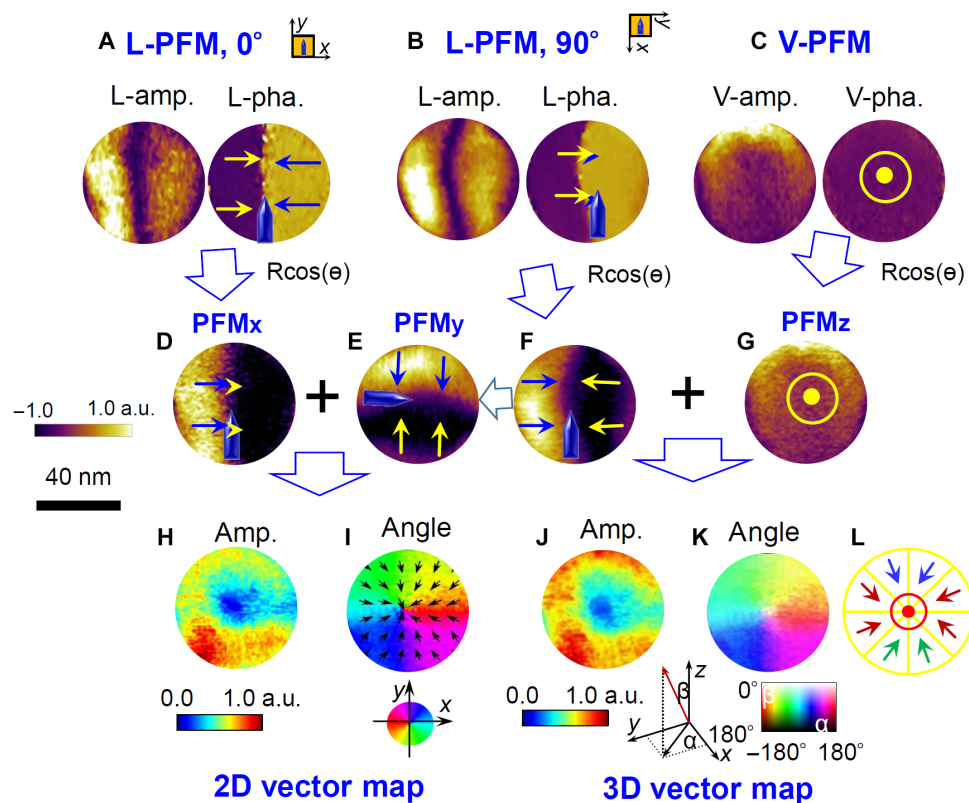

Fig. 2. 3D domain reconstruction using vector PFM analysis for a typical nanodomain inside a single nanodot. (**A** to **C**) The lateral PFM (L-PFM) amplitude and phase images with sample rotation for 0° (A) and 90° (B), along with the vertical PFM (V-PFM) images (C). (**D** to **G**) The piezoresponse images (PFM) for both the x, y, and z components derived from the combination of amplitude and phase images according to $R\cos(\theta)$ (R, amplitude; θ, phase angle), in which the x component of PFM (PFMx) (D) is converted from (A), (F) from (B), and the z component of PFM (PFMz) (G) from (C). The y component of PFM (PFMy) (E) is obtained by anticlockwise rotation of the image (F) for 90° so that the local PFM signals in (D), (E), and (G) are from the same locations. (**H** and **I**) 2D vector contour maps including the amplitude map (H) and phase angle map (I) converted from the combination of PFMx (D) and PFMy (E), presenting the lateral polarization distributions. (**J** and **K**) 3D vector map including the amplitude map (J) and phase angle map (K), derived from the combination of PFMx (D), PFMy (E), and PFMz (G). (**L**) Schematic diagram for the 3D domain structures. All the PFM images and vector maps share the same scale bar.
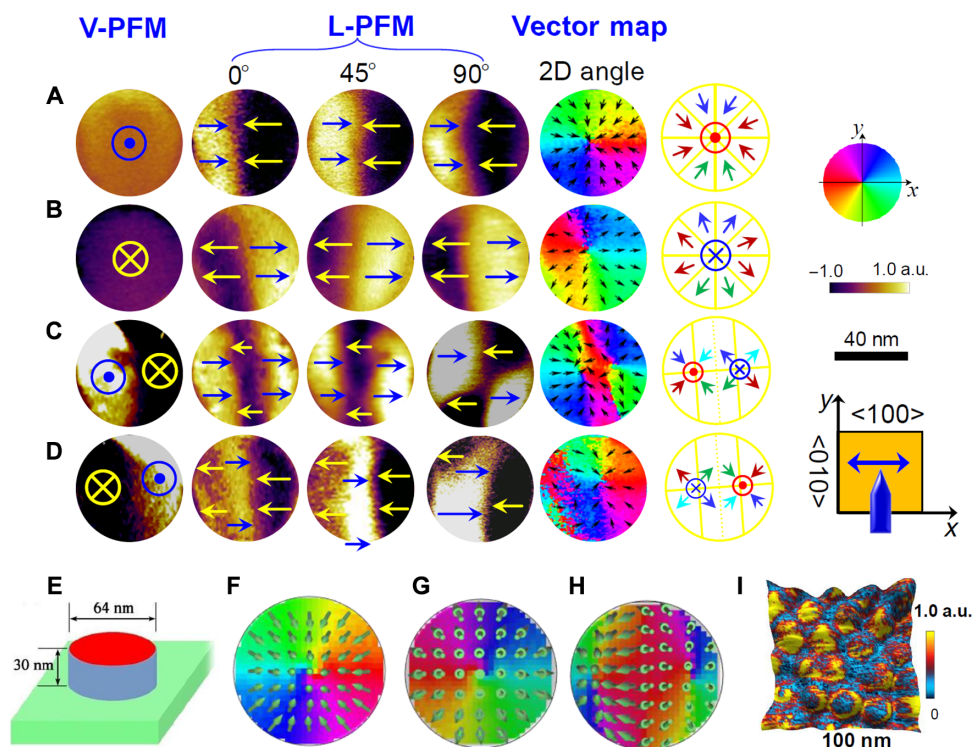
Fig. 3. Vector PFM images and vector maps, along with the simulated contours for some typical topological domains in the nanodots. (**A** to **D**) PFM images for the four typical domain structures frequently observed in the nanodots: center-convergent domain (A), center-divergent domain (B), double-center domain (C), and reverse double-center domain (D) that is equivalent to the double-center domain in (C). The micrographs from left to right are piezoresponse images derived from $R\cos(\theta)$ (R, amplitude; θ, the phase angle) for vertical PFM (PFMz) and lateral PFM for three sample rotation angles of 0° (PFMx), 45° (L-PFM along the <110> direction), and 90° (PFMy), as well as their corresponding 2D vector angle maps and schematic domain configurations. (**E**) Cylinder model for phase-field simulation of the center domains in the nanodots. (**F** to **H**) Three different polar vector contour maps derived from the simulation of the different charge distribution states: negative charge (F), positive charge (G), and half-positive and half-negative charge (H). The arrows in the simulated vector contours present the microscopic polarization directions, and the color scales show the angular distribution of lateral polarization. (**I**) STIM amplitude contrast map superimposed in 3D surface topology, indicating the nonuniform accumulation of mobile ionic charges. All the PFM images and vector maps are of the same size. All the PFM images (A to D) share the same scale and color bars.

vertical PFM image and the dark/bright contrast in the lateral PFM image, which turns out to be a radial center-divergent domain with radial outward polarizations. Type III (Fig. 3C) shows a double-contrast variation in the vertical PFM image, as well as a triple-contrast variation (bright/dark/bright) in the lateral image for angle 0° and a quadrant-domain contrast variation for angle 90°, corresponding to a double-center domain structure consisting of both a center-convergent domain and a divergent one. Type IV (Fig. 3D) is the reverse case of type III, and it is also a double-center domain structure consisting of a center-divergent domain and a convergent one, which can be considered as an equivalent state to type III. As a result, these domain structures can be reclassified into three types: center-convergent domain, center-divergent (convergent-reverse) domain, and double-center domain.

To complement the above analysis, we counted the percentages of different types of domain structures in an array of 238 nanodots at the virgin state without any electric poling. It was found that 55% of them are the radial center-convergent domains, ~14% are the radial center-divergent domains, ~24% are the double-center domains, and the rest are other types of domains (for example, single-domain structure).

DISCUSSION
The observations of these center domains instead of the earlier reported quadrant center domains are rather surprising, because the polarizations deviate from any of the predetermined eight <111> equivalent orientations for BFO. The formation of these domains is probably driven by the competitions among depolarization energy, polarization-strain coupling, and surface strain, all of which can greatly change the local anisotropy and thus the polarization distribution. Besides that, the possible nonuniform strain in the nanodots can generate the flexoelectric rotations that can drive the polarization away from their original directions (47, 48). In addition, the three types of center domain structures all have the head-to-head or tail-to-tail charge cores. This generates potentially high electrostatic energy, and one possible source favoring these structures is the surface and edge effects in low-dimensional systems, as predicted by Hong et al. (49) using the first-principles simulation. However, our system is much bigger (~60 nm) than the predicted one (a few unit cells in diameter), and the surface or edge effects may not provide the sufficient formation energy for center domains. Another possible reason is associated with the charge accumulation on the top surface, and this mechanism is supported by our phase-field simulation and additional experiments.

To mimic the experimental conditions, we modeled the nanodot as a nanoscale cylinder with a diameter of 64 nm and a height of 30 nm (Fig. 3E) and simulated it by phase-field simulation (the simulation details can be found in the Supplementary Materials). Figure 3 (F to H) shows the simulated polarization vector contours of the three BFO nanodots imposed with the three different charge distribution states at the top

surface: uniform negative charge (Fig. 3F), uniform positive charge (Fig. 3G), and combination of both negative and positive charges (Fig. 3H), resulting in different center domain states. It was found that the negative charges favor upward vertical polarizations with all in-plane polarizations inward, showing a center-convergent domain structures. For the positive charge state, the polarization distribution shows a center-divergent domain structure. In the case of half-positive and half-negative charge state, the nanodot shows two center domains, that is, a double-center domain structure. All the three domain structures match well with the topological domain states observed in the experiment.

The observed head-to-head or tail-to-tail charge domain cores are somewhat analogous to the charge domain walls, which can be stabilized by the charge accumulation from interior electrons, holes, ionic defects, or exterior absorbed charges adjacent to the walls, as summarized in a previous book chapter by Sluka et al. (7). In our case, these nanodots were fabricated from the BFO films deposited at a relatively low oxygen pressure (~2.0 Pa) and thus contained rather high-density oxygen vacancies and other charged carriers. As a result, the charge carriers can emigrate to the charge cores or domain heads/tails to stabilize the charge domain walls/cores. The free electrons from the ambient air can also be injected onto the surface close to the charge domain walls/cores, reducing the formation energy. This argument is also supported by the occurrence of many spontaneous charged domain walls in the abovementioned oxygen-deficient BFO films before the ion beam etching (see fig. S6A). In contrast, typical stripe-like domain patterns free of charged domain walls (for example, 71° domain walls) are dominant in the BFO films deposited at a much higher oxygen pressure of ~15 Pa (see fig. S6B). To visualize the possible charges on the nanodots, we carried out the scanning thermo-ionic microscopy (STIM) studies recently developed to map the distribution of ionic and other species mobile charges (50), as detailed in the Supplementary Materials. One example is the STIM amplitude mapping shown in Fig. 3I and fig. S7 superimposed on the 3D topology. It was observed that the STIM contrast is not uniform, with some dots showing bright contrast at the centers and others exhibiting dark contrast at the center together with bright contrast at the outer edges forming ring-like patterns. The former reflects the accumulation of mobile ions (likely oxygen vacancies in our cases) at the top center surface carrying positive charges, and the latter may be due to the accumulation of electron charges (dark contrast) at the top center and oxygen vacancies (bright contrast) at the outer edge or bottom of the dots. This nonuniform distribution of charges may act as an important stabilization force for the center domains.

The occurrence of the different charge distribution states and center domains may be attributed to the interactions between domain structures and mobile charges. Because the nanodot arrays were fabricated from the BFO film by ion beam etching, their charge distribution states can also be modulated by the domain structure (or the local ferroelectric polarization) of their parent film. After patterning, the as-fabricated small nanodots (size of ~60 nm) may inherit various polarization orientations or different types of charged walls from the film. If the nanodots have purely upward vertical component of polarization together with head-to-head charge domain walls at initial states, the negative charges can be attracted to the top surfaces of the nanodots to screen the polarization, leading to the negative charge states. In contrast, the positive charge states form in the nanodots with purely downward vertical component of polarization along with tail-to-tail charge domains, and the mixed charge states occur on those nanodots containing both upward and downward polarization domains, as well as charge domain walls. After a reconstruction of domain structure of these nanodots, they can evolve into different types of center domains in the final stage.

It is understandable that a direct probing of the whole dynamic process argued above can be challenging at the current stage, yet we can still obtain some indirect evidence. For instance, this can be further supported by the surface potential maps derived from the polarization bond charges for the three different center domain states (see fig. S8, A to C). To compensate for the potential variation, the mobile charges migrate to the low-energy potential regions, leading to the different charge occupation/distribution states. It should be mentioned that, to support this argument, we have used a simplified model to illustrate the formation mechanism of the center domains in this work. In a real system, the charge distribution states can be more nonuniform, and they tend to concentrate toward the cores of the center domains (see fig. S8, D and E). Besides, mobile charges may also occupy on the edges or interior bodies of the nanodots, which can further reduce the formation energy of center domains.

In addition, other factors can also affect the formation of center domains. To understand the geometric effect, we compare the domain structures between an oxygen-deficient parent BFO film and the nanodots derived from it. By carefully examining the domain patterns of the film (see vector map in fig. S6A), we can find many stripe-like charge domain walls, along with one or two exceptional center domains shown among the stripe-like domain pattern. However, once the film was etched into an array of nanodots with a lateral size of ~60 nm, high-density center domains can be observed in the array with only several exceptions, as have been analyzed previously. For nanodots with a relatively larger size (~300 nm; see fig. S9A), one can see quite a few center domains with some extent of distortion compared to the ideal one in the same area. Therefore, it is obvious that there occurs an apparent domain reconstruction after patterning of the BFO films into nanodot arrays, and the geometric parameters play an important role.

The effects of fabrication methods were also examined, by comparing the three samples derived from different fabrication methods (see fig. S9). As mentioned above, for the nanodots (~300 nm) derived from the same method use in this work (see fig. S9A), we can find the distorted center domains. In contrast, if the nanodot arrays are derived from the less oxygen-deficient BFO film with a charge-free stripe domain pattern, they can more or less maintain the stripe-like domains instead of the center domains (see fig. S9B). Finally, we also present an additionally prepared sample containing a square-shape BFO nanodot (~400 nm in lateral size) array fabricated by porous AAO template–assisted pulsed laser deposition (PLD) method, wherein each individual nanodot in the array contains a pure center-convergent domain (see fig. S9C). The occurrence of these pure center-convergent domains over a large array may be associated with the fact that the vertical components of polarization for all the nanodots are purely upward self-polarized, which tend to attract negative charges on the top surfaces and stabilize the center-convergent domains. The above observations indicated that the nanodomains are greatly dependent on the level of mobile charges, geometric parameters, and fabrication techniques, thus creating an opportunity for tailoring the different topological defects (for example, center domain and vortex states) for on-demand applications by properly tuning these parameters.

Equally exciting is that these center domains can be reversibly switched. Figure 4 (A to D) shows the V-pha. and L-pha. images for a nanodot array, in which three of the individual nanodots were subjected to electric pulses by fixing the AFM probe on the selected individual nanodots. Upon applying an electric pulse of +8 V, one can see that the domain can be switched into the center-divergent domain, whereas applying a pulse of −8 V converts the center-divergent domain
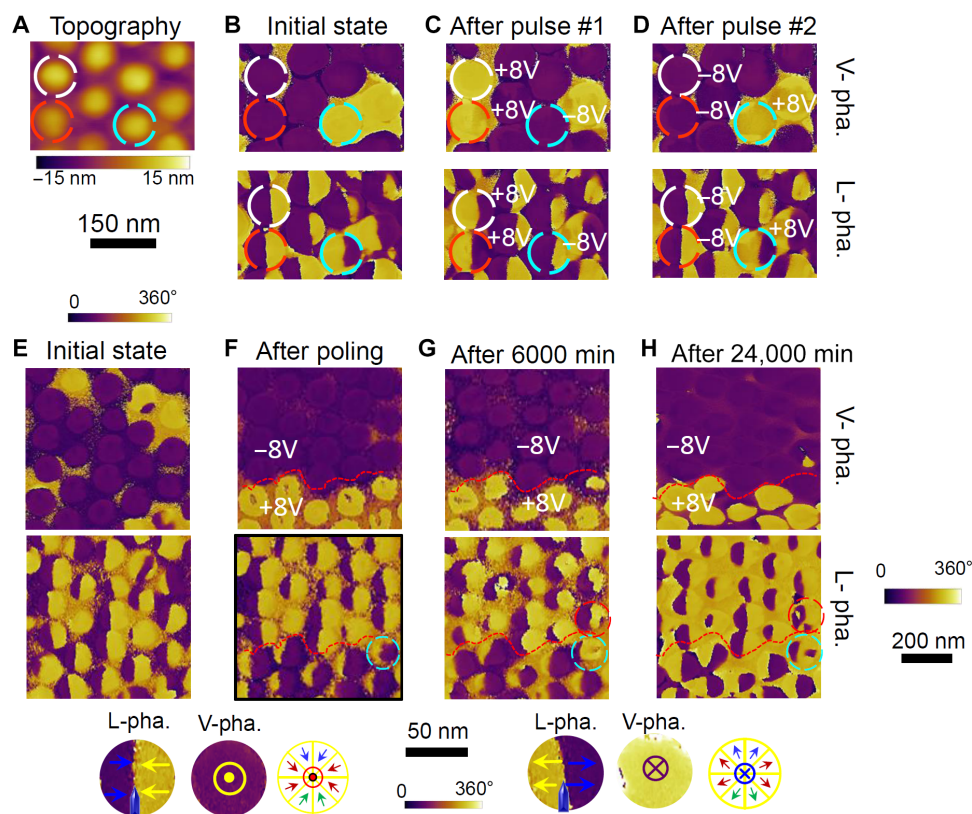
Fig. 4. Electric switching behaviors and retention properties for an array of center domains. (A to D) The topology and PFM images for a nanodot array illustrating the reversible switching of center domains triggered by applying pulsed electric fields on individual dots, including the topological image (A) and the PFM vertical (top) and lateral (bottom) phase images at the initial state (B), after the first set of electric pulses (C), and after the second set of electric pulses (D). (E to H) PFM images showing the electric switching of center domains by scanning electric bias and the retention properties for the switched center domains, for the initial state (E), the just switching state (F), after a retention duration of 6000 min (G), and after an elongated retention duration of 24,000 min (H). The circles in (G) and (H) indicate the contrast changes in certain nanodots during the retention test. The insets below the panels illustrate the characteristic contrasts in the L-pha. and V-pha. images for center-convergent (left) and center-divergent (right) domains, respectively. PFM images (A) to (E) share the same scale and color bars, and PFM images (F) to (H) share the same scale and color bars.

to the center-convergent domain, as indicated by the complete reversal of contrast patterns in both the V-pha. and L-pha. images for the selected nanodots (see Fig. 4, B and C). These reversed center domains can also be switched back to their initial states by applying another set of electric pulses with opposite polarization (see Fig. 4, C and D), indicating that the switching is reversible and individually addressable. The domain switching behavior for an array of nanodots triggered by scanning electric bias and their retention properties are shown in Fig. 4 (E to H). It was found that applying two different sets of scanning bias voltages (±8 V) via the AFM probe on an array of nanodots produces two distinct regions with rather uniform center-convergent domains (with upward polarization) for +8 V and center-divergent domains (with upward polarization) for −8 V. After a retention duration of 6000 min, the center domains remained nearly unchanged, except that one at the border was switched from center-convergent back to divergent domain. After an even longer duration (24,000 min), most of the topologic center domains remain unchanged. This suggests that the center domains are rather robust in ambient conditions yet reversibly switchable under electric field. This also enables further manipulation of these topological domain states by electric field, which is promising for applications in high-density devices, for example, nonvolatile memories.

In summary, we have observed different types of spontaneous ferroelectric topological domain states in multiferroic BFO nanodot arrays. The domain configurations in the nanodot array were examined by vector PFM analysis, which reveals the existence of center-convergent domain, reverse center (center-divergent) domain, and double-center domains. These domain structures exist spontaneously in the as-fabricated virgin states, stabilized by the accumulation of charge on the top surface, as supported by our phase-field simulations and STIM characterization. Furthermore, these topological domains are rather stable and can be effectively and reversibly switched by electric fields, which is promising for potential applications in high-density memory devices.

MATERIALS AND METHODS
Fabrication of BFO nanodot array
The nanodot arrays were fabricated by a sacrificed ultrathin (~300 nm) AAO template etching technique, and the details can be found in our previous work (37). The simplified procedure is shown fig. S2. In brief, an epitaxial BFO film (~100 nm thick) with a ~50-nm SrRuO$_3$ bottom electrode layer was first grown on a (001)-oriented SrTiO$_3$ substrate by PLD. Then, an ultrathin (~300 nm) AAO membrane mask (refer to the Supplementary Materials) was transferred onto the BFO film surface, followed by the Ar$^+$ ion beam etching. The ion beam gradually changed the shapes of both mask and film and developed an epitaxial nanodot

array. Finally, the mask was removed by mechanical method, and the attractive nanostructures were obtained. The as-prepared nanodots maintain both epitaxial structures and good electrical properties close to their parent films. This procedure is reproducible, and the as-prepared samples for subsequent characterizations show good consistency with each other.

Structure, PFM, and STIM characterizations

The topographic images of the as-prepared nanodot arrays were measured by AFM at contact mode (Cypher, Asylum Research). The crystallinity of nanodots was characterized by XRD (X'Pert PRO, PANalytical). The ferroelectric domain structures of these nanodots were characterized by PFM (Asylum Cypher) using conductive probes (Arrow EFM, NanoWorld). The local piezoresponse loop measurements were carried out by fixing the PFM probe on a selected nanodot and then applying a triangle-square waveform accompanied by an ac-driven voltage via the conductive PFM probe. To improve the PFM sensitivity, we adopted a dual-frequency resonance-tracking technique also provided by Asylum Research (36). The vector PFM function of our AFM unit allows simultaneous mapping of the vertical (out-of-plane) and lateral (in-plane) amplitude (V-amp. and L-amp.) and phase (V-pha. and L-pha.) signals from the nanodots one by one. To determine the 3D domain structures, we conducted both the vertical and lateral PFM images for different in-plane sample rotation angles. In proceeding, we marked the sample before the rotations so that the same scanned area can be tracked. The implementation of STIM (50) here uses an Asylum Research MFP-3D AFM equipped with Anasys ThermaLever AN2-300 thermal probe, and the technical details can also be found in the Supplementary Materials.

Phase-field simulation details

We simulated the nanodot as a cylinder surrounded by vacuum, as shown in Fig. 3E. We chose a mesh size of $x_0 = y_0 = 2$ nm and $z_0 = 0.6$ nm so that a $64 \times 64 \times 50$ mesh corresponds to a 128 nm × 128 nm × 30 nm model. The diameter of the cylinder for the nanodot is 64 nm, and the height is 30 nm inside the simulation mesh. At the bottom and top of the nanodot, the short- and open-circuit boundary conditions are applied, respectively. This type of electric boundary condition is consistent with the experimental setup that the nanodot is grown on a bottom electrode. To simulate the different charge distribution states, we applied the charge on the top surface of the nanodots for all the three different states: uniform positive charge, uniform negative charge, and combination of positive and negative charges. The evolution of polarization in BFO nanodots is studied by phase-field simulations, which are based on the time-dependent Ginzburg-Landau equation. The Landau-Devonshire energy of BFO is expanded as a fourth-order polynomial using the parameters adopted from previous studies (51, 52). More simulation details can also be found in the Supplementary Materials.

SUPPLEMENTARY MATERIALS

Supplementary material for this article is available at http://advances.sciencemag.org/cgi/content/full/3/8/e1700919/DC1

Nanoporous AAO membrane mask fabrication
Scanning thermo-ionic microscopy
Phase-field simulation details and parameters
table S1. The coefficients used in phase-field simulations.
fig. S1. Schematic diagrams for different 1D topologically polar domain.
fig. S2. Schematic procedures for the fabrication and PFM characterization of BFO nanodot array sample.
fig. S3. PFM images for the nanodot array after poling by scanning bias voltages of ±8 V.
fig. S4. 3D PFM images for a nanodot array.
fig. S5. Single-dot PFM images for four typical topologic domains.
fig. S6. A comparison of domain structures between an oxygen-deficient BFO film and a less oxygen-deficient film.
fig. S7. STIM images of a nanodot array in this work.
fig. S8. Surface potential maps and charge distribution states for different center domains.
fig. S9. The domain structures for nanodots with a relatively larger lateral size (~300 nm) derived from three different methods.

REFERENCES AND NOTES

1. G. Catalan, J. Seidel, R. Ramesh, J. F. Scott, Domain wall nanoelectronics. *Rev. Mod. Phys.* **84**, 119–156 (2012).
2. N. D. Mermin, The topological theory of defects in ordered media. *Rev. Mod. Phys.* **51**, 591–648 (1979).
3. I. I. Naumov, L. Bellaiche, H. X. Fu, Unusual phase transitions in ferroelectric nanodisks and nanorods. *Nature* **432**, 737–740 (2004).
4. J. Seidel, R. K. Vasudevan, N. Valanoor, Topological structures in multiferroics—Domain walls, skyrmions and vortices. *Adv. Electron. Mater.* **2**, 1500292 (2016).
5. Y. Nahas, S. Prokhorenko, L. Louis, Z. Gui, I. Kornev, L. Bellaiche, Discovery of stable skyrmionic state in ferroelectric nanocomposites. *Nat. Commun.* **6**, 8542 (2015).
6. M.-G. Han, Y. Zhu, L. Wu, T. Aoki, V. Volkov, X. Wang, S. C. Chae, Y. S. Oh, S.-W. Cheong, Ferroelectric switching dynamics of topological vortex domains in a hexagonal manganite. *Adv. Mater.* **25**, 2415–2421 (2013).
7. T. Sluka, P. Bednyakov, P. Yudin, A. Crassous, A. Tagantsev, in *Topological Structures in Ferroic Materials*, vol. 228 of *Springer Series in Materials Science*, J. Seidel, Ed. (Springer, ed. 1, 2016), chap. 5.
8. S. Dong, J.-M. Liu, S.-W. Cheong, Z. Ren, Multiferroic materials and magnetoelectric physics: Symmetry, entanglement, excitation, and topology. *Adv. Phys.* **64**, 519–626 (2015).
9. R. K. Vasudevan, Y.-C. Chen, H.-H. Tai, N. Balke, P. Wu, S. Bhattacharya, L. Q. Chen, Y.-H. Chu, I.-N. Lin, S. V. Kalinin, V. Nagarajan, Exploring topological defects in epitaxial BiFeO₃ thin films. *ACS Nano* **5**, 879–887 (2011).
10. C. T. Nelson, B. Winchester, Y. Zhang, S.-J. Kim, A. Melville, C. Adamo, C. M. Folkman, S.-H. Baek, C.-B. Eom, D. G. Schlom, L.-Q. Chen, X. Pan, Spontaneous vortex nanodomain arrays at ferroelectric heterointerfaces. *Nano Lett.* **11**, 828–834 (2011).
11. C.-L. Jia, K. W. Urban, M. Alexe, D. Hesse, I. Vrejoiu, Direct observation of continuous electric dipole rotation in flux-closure domains in ferroelectric Pb(Zr,Ti)O₃. *Science* **331**, 1420–1423 (2011).
12. Y. L. Tang, Y. L. Zhu, X. L. Ma, A. Y. Borisevich, A. N. Morozovska, E. A. Eliseev, W. Y. Wang, Y. J. Wang, Y. B. Xu, Z. D. Zhang, S. J. Pennycook, Observation of a periodic array of flux-closure quadrants in strained ferroelectric PbTiO₃ films. *Science* **348**, 547–551 (2015).
13. A. K. Yadav, C. T. Nelson, S. L. Hsu, Z. Hong, J. D. Clarkson, C. M. Schlepüetz, A. R. Damodaran, P. Shafer, E. Arenholz, L. R. Dedon, D. Chen, A. Vishwanath, A. M. Minor, L. Q. Chen, J. F. Scott, L. W. Martin, R. Ramesh, Observation of polar vortices in oxide superlattices. *Nature* **530**, 198–201 (2016).
14. T. Choi, Y. Horibe, H. T. Yi, Y. J. Choi, W. Wu, S.-W. Cheong, Insulating interlocked ferroelectric and structural antiphase domain walls in multiferroic YMnO₃. *Nat. Mater.* **9**, 253–258 (2010).
15. S.-Z. Lin, X. Wang, Y. Kamiya, G.-W. Chern, F. Fan, D. Fan, B. Casas, Y. Liu, V. Kiryukhin, W. H. Zurek, C. D. Batista, S.-W. Cheong, Topological defects as relics of emergent continuous symmetry and Higgs condensation of disorder in ferroelectrics. *Nat. Phys.* **10**, 970–977 (2014).
16. F.-T. Huang, B. Gao, J.-W. Kim, X. Luo, Y. Wang, M.-W. Chu, C.-K. Chang, H.-S. Sheu, S.-W. Cheong, Topological defects at octahedral tilting plethora in bi-layered perovskites. *npj Quantum Mater.* **1**, 16017 (2016).
17. N. Balke, B. Winchester, W. Ren, Y.-H. Chu, A. N. Morozovska, E. A. Eliseev, M. Huijben, R. K. Vasudevan, P. Maksymovych, J. Britson, S. Jesse, I. Kornev, R. Ramesh, L. Bellaiche, L.-Q. Chen, S. V. Kalinin, Enhanced electric conductivity at ferroelectric vortex cores in BiFeO₃. *Nat. Phys.* **8**, 81–88 (2012).
18. N. Balke, S. Choudhury, S. Jesse, M. Huijben, Y. H. Chu, A. P. Baddorf, L. Q. Chen, R. Ramesh, S. V. Kalinin, Deterministic control of ferroelastic switching in multiferroic materials. *Nat. Nanotechnol.* **4**, 868–875 (2009).
19. Y.-C. Chen, G.-F. Wang, H.-H. Tai, J.-W. Chen, Y.-C. Huang, J.-C. Yang, Y.-H. Chu, Non-volatile domain nucleation and growth in multiferroic BiFeO₃ films. *Nanotechnology* **22**, 254030 (2011).
20. A. Gruverman, A. Kholkin, Nanoscale ferroelectrics: Processing, characterization and future trends. *Rep. Prog. Phys.* **69**, 2443–2474 (2006).
21. J. F. Scott, Applications of modern ferroelectrics. *Science* **315**, 954–959 (2007).
22. H. Han, Y. Kim, M. Alexe, D. Hesse, W. Lee, Nanostructured ferroelectrics: Fabrication and structure–property relations. *Adv. Mater.* **23**, 4599–4613 (2011).

23. A. Gruverman, D. Wu, H.-J. Fan, I. Vrejoiu, M. Alexe, R. J. Harrison, J. F. Scott, Vortex ferroelectric domains. *J. Phys. Condens. Matter* **20**, 342201 (2008).

24. A. Schilling, D. Byrne, G. Catalan, K. G. Webber, Y. A. Genenko, G. S. Wu, J. F. Scott, J. M. Gregg, Domains in ferroelectric nanodots. *Nano Lett.* **9**, 3359–3364 (2009).

25. L. J. McGilly, A. Schilling, J. M. Gregg, Domain bundle boundaries in single crystal BaTiO₃ lamellae: Searching for naturally forming dipole flux-closure/quadrupole chains. *Nano Lett.* **10**, 4200–4205 (2010).

26. R. G. P. McQuaid, L. J. McGilly, P. Sharma, A. Gruverman, J. M. Gregg, Mesoscale flux-closure domain formation in single crystal BaTiO₃. *Nat. Commun.* **2**, 404 (2011).

27. B. J. Rodriguez, X. S. Gao, L. F. Liu, W. Lee, I. I. Naumov, A. M. Bratkovsky, D. Hesse, M. Alexe, Vortex polarization states in nanoscale ferroelectric arrays. *Nano Lett.* **9**, 1127–1131 (2009).

28. G. Catalan, J. F. Scott, Physics and applications of bismuth ferrite. *Adv. Mater.* **21**, 2463–2485 (2009).

29. D. Sando, A. Barthélémy, M. Bibes, BiFeO₃ epitaxial thin films and devices: Past, present and future. *J. Phys. Condens. Matter* **26**, 473201 (2014).

30. D. Chen, Z. Chen, Q. He, J. D. Clarkson, C. R. Serrao, A. K. Yadav, M. E. Nowakowski, Z. Fan, L. You, X. Gao, D. Zeng, L. Chen, A. Y. Borisevich, S. Salahuddin, J.-M. Liu, J. Bokor, Interface engineering of domain structures in BiFeO₃ thin films. *Nano Lett.* **17**, 486–493 (2017).

31. S. Wintz, C. Bunce, A. Neudert, M. Körner, T. Strache, M. Buhl, A. Erbe, S. Gemming, J. Raabe, C. Quitmann, J. Fassbender, Topology and origin of effective spin meron pairs in ferromagnetic multilayer elements. *Phys. Rev. Lett.* **110**, 177201 (2013).

32. G. Tian, L. Zhao, Z. Lu, J. Yao, H. Fan, Z. Fan, Z. Li, P. Li, D. Chen, X. Zhang, M. Qin, M. Zeng, Z. Zhang, J. Dai, X. Gao, J.-M. Liu, Fabrication of high-density BiFeO₃ nanodot and anti-nanodot arrays by anodic alumina template-assisted ion beam etching. *Nanotechnology* **27**, 485302 (2016).

33. W. Lee, R. Ji, U. Gösele, K. Nielsch, Fast fabrication of long-range ordered porous alumina membranes by hard anodization. *Nat. Mater.* **5**, 741–747 (2006).

34. W. Lee, H. Han, A. Lotnyk, M. A. Schubert, S. Senz, M. Alexe, D. Hesse, S. Baik, U. Gösele, Individually addressable epitaxial ferroelectric nanocapacitor arrays with near Tb inch⁻² density. *Nat. Nanotechnol.* **3**, 402–407 (2008).

35. G. Tian, F. Zhang, J. Yao, H. Fan, P. Li, Z. Li, X. Song, X. Zhang, M. Qin, M. Zeng, Z. Zhang, J. Yao, X. Gao, J. Liu, Magnetoelectric coupling in well-ordered epitaxial BiFeO₃/CoFe₂O₄/SrRuO₃ heterostructured nanodot array. *ACS Nano* **10**, 1025–1032 (2016).

36. L. Zhao, Z. Lu, F. Zhang, G. Tian, X. Song, Z. Li, K. Huang, Z. Zhang, M. Qin, S. Wu, X. Lu, M. Zeng, X. Gao, J. Dai, J.-M. Liu, Current rectifying and resistive switching in high density BiFeO₃ nanocapacitor arrays on Nb-SrTiO₃ substrates. *Sci. Rep.* **5**, 9680 (2015).

37. X. S. Gao, B. J. Rodriguez, L. Liu, B. Birajdar, D. Pantel, M. Ziese, M. Alexe, D. Hesse, Microstructure and properties of well-ordered multiferroic Pb(Zr,Ti)O₃/CoFe₂O₄ nanocomposites. *ACS Nano* **4**, 1099–1107 (2010).

38. Y. H. Chu, T. Zhao, M. P. Cruz, Q. Zhan, P. L. Yang, L. W. Martin, M. Huijben, C. H. Yang, F. Zavaliche, H. Zheng, R. Ramesh, Ferroelectric size effects in multiferroic BiFeO₃ thin films. *Appl. Phys. Lett.* **90**, 252906 (2007).

39. J. Wang, J. B. Neaton, H. Zheng, V. Nagarajan, S. B. Ogale, B. Liu, D. Viehland, V. Vaithyanathan, D. G. Schlom, U. V. Waghmare, N. A. Spaldin, K. M. Rabe, M. Wuttig, R. Ramesh, Epitaxial BiFeO₃ multiferroic thin film heterostructures. *Science* **299**, 1719–1722 (2003).

40. B. J. Rodriguez, C. Callahan, S. V. Kalinin, R. Proksch, Dual-frequency resonance-tracking atomic force microscopy. *Nanotechnology* **18**, 475504 (2007).

41. M. Abplanalp, L. M. Eng, P. Günter, Mapping the domain distribution at ferroelectric surfaces by scanning force microscopy. *Appl. Phys. A* **66**, S231–S234 (1998).

42. A. Roelofs, U. Böttger, R. Waser, F. Schlaphof, S. Trogisch, L. M. Leng, Differentiating 180° and 90° switching of ferroelectric domains with three-dimensional piezoresponse force microscopy. *Appl. Phys. Lett.* **77**, 3444–3446 (2000).

43. J. T. Heron, J. L. Bosse, Q. He, Y. Gao, M. Trassin, L. Ye, J. D. Clarkson, C. Wang, J. Liu, S. Salahuddin, D. C. Ralph, D. G. Schlom, J. Íñiguez, B. D. Huey, R. Ramesh, Deterministic switching of ferromagnetism at room temperature using an electric field. *Nature* **516**, 370–373 (2014).

44. B. J. Rodriguez, A. Gruverman, A. I. Kingon, R. J. Nemanich, J. S. Cross, Three-dimensional high-resolution reconstruction of polarization in ferroelectric capacitors by piezoresponse force microscopy. *J. Appl. Phys.* **95**, 1958–1962 (2004).

45. S. V. Kalinin, A. Gruverman, Piezoresponse force microscopy and recent advances in nanoscale studies of ferroelectrics. *J. Mater. Sci.* **41**, 107–116 (2006).

46. J. Li, J.-F. Li, Q. Yu, Q. N. Chen, S. Xie, Strain-based scanning probe microscopies for functional materials, biological structures, and electrochemical systems. *J. Materiomics* **1**, 3–21 (2015).

47. I. Naumov, A. M. Bratkovsky, Unusual polarization patterns in flat epitaxial ferroelectric nanoparticles. *Phys. Rev. Lett.* **101**, 107601 (2008).

48. G. Catalan, A. Lubk, A. H. G. Vlooswijk, E. Snoeck, C. Magen, A. Janssens, G. Rispens, G. Rijnders, D. H. A. Blank, B. Noheda, Flexoelectric rotation of polarization in ferroelectric thin films. *Nat. Mater.* **10**, 963–967 (2011).

49. J. Hong, G. Catalan, D. N. Fang, E. Artacho, J. F. Scott, Topology of the polarization field in ferroelectric nanowires from first principles. *Phys. Rev. B* **81**, 172101 (2010).

50. A. Eshghinejad, E. N. Esfahani, P. Wang, S. Xie, T. C. Geary, S. B. Adler, J. Li, Scanning thermo-ionic microscopy for probing local electrochemistry at the nanoscale. *J. Appl. Phys.* **119**, 205110 (2016).

51. J. X. Zhang, Y. L. Li, Y. Wang, Z. K. Liu, L. Q. Chen, Y. H. Chu, F. Zavaliche, R. Ramesh, Effect of substrate-induced strains on the spontaneous polarization of epitaxial BiFeO₃ thin films. *J. Appl. Phys.* **101**, 114105 (2007).

52. J. J. Wang, J. Hu, R. Peng, Y. Gao, Y. Shen, L. Q. Chen, C. W. Nan, Magnetization reversal by out-of-plane voltage in BiFeO₃-based multiferroic heterostructures. *Sci. Rep.* **5**, 10459 (2015).